PAPER

Check for updates

A TICT mechanism-based viscosity fluorescent probe for monitoring viscosity in inflammatory cells†

Song Han, [ID] Xinying Jing, [ID] Hui Peng and Weiying Lin [ID] *

Viscosity, as a fundamental biophysical parameter of cellular microenvironments, critically regulates physiological processes, including molecular transport and signal transduction. Lysosomes, functioning as pivotal organelles, orchestrate essential biological activities such as macromolecular degradation and autophagic flux. Aberrant viscosity fluctuations disrupt the substrate delivery within lysosomal enzymatic activation zones, precipitating accumulation of undegraded metabolites and subsequent release of inflammatory mediators, ultimately contributing to chronic inflammatory diseases. Consequently, developing high-performance probes capable of real-time lysosomal viscosity monitoring is imperative for the prevention, diagnosis and therapeutic intervention of inflammatory diseases. We developed a lysosome-targeted fluorescent probe, **LTP-H**, based on the TICT mechanism. The probe demonstrated a linear correlation between fluorescence intensity at 650 nm and medium viscosity ($R^2 = 0.995$), exhibiting a 93-fold viscosity response ratio with robust stability against solvent polarity variations, pH fluctuations, and biological interferents. Density functional theory calculations corroborated the TICT response mechanism. Based on the strong hydrophobic property of the triphenylamine group, the **LTP-H** probe achieved pH-independent lysosomal targeting through a hydrophobicity-mediated membrane localization mechanism ($p = 0.90$). Successful application in monitoring viscosity dynamics within inflammatory cellular models and pharmacologically manipulated zebrafish demonstrated its utility as a molecular tool for investigating microenvironmental viscosity in inflammatory diseases.

1. Introduction

Viscosity plays a pivotal role in governing mechanobiological interactions within cellular and extracellular microdomains, which profoundly impacts a series of physiological activities such as molecular and protein transport, intracellular signalling, biomolecule interactions and metabolic diffusion.[1–5] There is a close and complex intrinsic link between cell viscosity and inflammation: when inflammation occurs, a series of pathological processes are triggered, such as cell stimulation by pathogens, injury signals, and the production of large amounts of inflammatory factors. These actions lead to the activation of intracellular signalling pathways, which trigger remodelling of the cytoskeleton, and the aggregation of actin to make the intracellular structure denser, limiting molecular movement, resulting in the elevation of cellular viscosity.[6–10] At the same time, inflammation-induced oxidative stress causes lipid

peroxidation, protein crosslinking and other damage. Hence, intracellular substance transport is blocked, further increasing viscosity. This results in the abnormal performance of cellular actions, such as interfering with the transmembrane transport of substances and blockade of intracellular signalling. These actions make it difficult to effectively control inflammatory reactions. Hence, a "vicious circle" is formed that continues to promote the development of inflammation, aggravates tissue damage, and causes a number of negative impacts on the health of the organism.[11–17] Therefore, monitoring changes in intracellular viscosity is critical for the early recognition and identification of inflammatory processes to predict disease progression and improve effective treatment.[18,19]

As pivotal cellular organelles, lysosomes regulate signal transduction, autophagy processes and cellular homeostasis to sustain core physiological functions. Lysosomes also form dynamic interaction networks with the endoplasmic reticulum, mitochondria and other organelles.[20,21] Accumulating evidence has demonstrated a close association between lysosomal dysfunction and chronic inflammatory states. Lysosomal impairment induces intracellular environmental destabilisation and exacerbates inflammation-linked pathological progression, with inflammation-driven aberrant autophagy specifically modulating lysosomal viscosity.[22–24] Consequently, lysosomal

Institute of Optical Materials and Chemical Biology, Guangxi Key Laboratory of Electrochemical Energy Materials, School of Chemistry and Chemical Engineering, Guangxi University, Nanning, Guangxi 530004, P. R. China. E-mail: weiyinglin2013@163.com
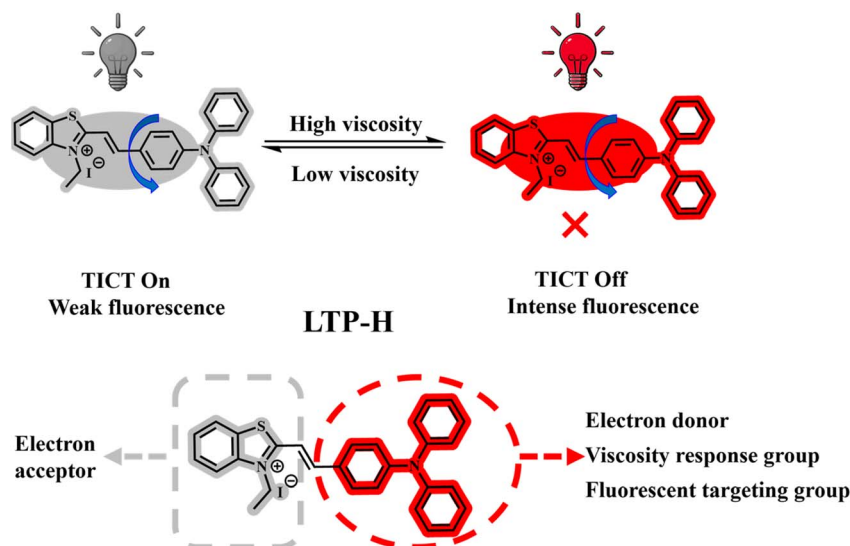
Scheme 1 Design of the probe **LTP-H** to measure viscosity changes.

monitoring and intracellular viscosity visualisation hold significant value in medical research for the assessment, diagnosis and therapeutic management of inflammatory and associated disease states. In recent years, fluorescent probes have attracted much attention in the field of bioanalysis due to their simplicity, non-invasive detection capability, high sensitivity and good biocompatibility,[25–30] and have shown great potential for application in the monitoring of important physiological parameters such as organismal viscosity, pH, and biothiols.[31–35] In 2024, Zhang *et al.*[36] developed a near-infrared probe **WZ-V** with a large Stokes shift, enabling liver injury monitoring through viscosity response behaviour. Concurrently, Wang *et al.*[37] designed the D–π–A structured probes **PTPA-B** and **CPTPA-B** based on the TICT mechanism, achieving high selectivity for human serum albumin (HSA) detection. Chao *et al.*[38] subsequently synthesised a multifunctional xanthine-core probe, **CCA**, for simultaneous quantitative detection of viscosity, polarity, sulfur dioxide, and hydrogen peroxide, with the biological application of distinguishing normal from cancer cells *via* cellular viscosity. In 2025, Hao *et al.*[39] developed a lysosome-targeted two-photon probe, **VFLyso**, based on a DIC core scaffold. Building upon inflammatory cell viscosity visualisation, this probe was further adapted to monitor lysosomal viscosity changes in murine fatty liver models and track viscosity dynamics in zebrafish. Although these probes exhibit commendable photophysical and biological characteristics, their structural and synthetic complexity, coupled with pH-dependent lysosomal targeting mechanisms that are prone to inducing alkalinisation effects,[40–42] present notable limitations. The present study addressed these constraints through the development of a lysosomal viscosity-responsive fluorescent probe featuring simplified synthetic protocols and pH-independent targeting functionality.

The synthetic design of the probe was based on the TICT mechanism, with **LTP-H** relying on the electron-donating properties and dynamic rotational conformation of triphenylamine (TPA). This configuration incorporated benzothiazolium iodide as the electron-accepting unit, enabling highly sensitive viscosity monitoring in both *ex vivo* and *in vivo* systems without interference from microenvironmental factors (Scheme 1). In bioimaging applications, the lysosomal targeting mechanism achieved precise localization through hydrophobic-driven penetration of the TPA moiety, operating independently of traditional pH-dependent modes. Systematic validation through drug-induced cellular inflammation models and zebrafish *in vivo* viscosity imaging demonstrated cross-scale inflammatory monitoring spanning *in vitro* to *in vivo* environments. Therefore, this probe functioned as a molecular tool for detecting inflammation in biological systems, with potential applications in diagnosing physiological states, analysing pathological processes, and investigating mechanisms of inflammation-related disorders.

2. Experimental component

2.1 Reagents and instruments

Unless otherwise stated, all raw materials were purchased directly from the supplier without secondary processing. The water was double-deionised and the solvents employed were of analytical purity procured from certified suppliers. Chromatography-grade solvents were specifically chosen for the spectral characterisation to eliminate factors that could interfere with the stability of the spectral baseline. Comprehensive details regarding the laboratory equipment and biological samples utilised in the experiments are provided in the ESI.†

2.2 Synthesis and characterization of the probe LTP-H

The synthetic pathway and mechanism underlying the response of the probe **LTP-H** are illustrated in ESI Scheme S1.† The detailed procedures for synthesising compound 1 and compound 2 are provided in the ESI.† Compound 1 (610.00 mg, 2.00 mmol) underwent dissolution in anhydrous ethanol (6 mL)

and was stirred at 80 °C for 1 h. The dissolved compound was added to compound 2 (364.00 mg, 1.33 mmol) and catalyst piperidine (100 μL), heated to 85 °C, followed by condensation and refluxing for 8 h with progress monitored by TLC. Upon solvent removal under reduced pressure, the crude extract was purified using column chromatography with the DCM/MeOH (20 : 1) gradient elution system, yielding **LTP-H** as a purple-red solid (447.00 mg, 60% yield). ^{1}H NMR (600 MHz, chloroform-d) δ 8.79 (d, J = 4.4 Hz, 1H), 8.12 (s, 1H), 8.05 (d, J = 8.1 Hz, 1H), 8.01 (d, J = 8.3 Hz, 1H), 7.96 (d, J = 7.7 Hz, 1H), 7.72 (t, J = 6.9 Hz, 1H), 7.58 (d, J = 7.0 Hz, 1H), 7.55 (d, J = 8.3 Hz, 1H), 7.51 (d, J = 8.6 Hz, 2H), 7.47 (t, J = 8.2 Hz, 1H), 7.31–7.27 (m, 3H), 7.16 (dd, J = 15.2, 8.0 Hz, 4H), 7.08–7.03 (m, 2H), 6.62 (d, J = 8.2 Hz, 1H), 2.73 (s, 2H), 1.42 (s, 3H). ^{13}C NMR (151 MHz, CDCl$_3$) δ 190.44, 152.47, 149.15, 145.85, 139.81, 131.43, 130.48, 130.17, 127.90, 127.40, 126.80, 126.65, 125.99, 124.75, 121.66, 121.18, 112.20, 43.07, 13.51. HRMS (ESI): calcd for C29H25N2S$^+$, [M]$^+$, m/z, 433.1738, found: 433.1739.

Additional synthesis details are shown in Scheme S1.†

3. Results and discussion

3.1 Rational design of LTP-H

The probe **LTP-H** is based on the TICT mechanism. It can be constructed through the Vilsmeier and iodine substitution reactions to form a D–π–A molecular architecture with triphenylamine (TPA) as the electron-donor and benzothiazole as the electron-acceptor. Its core design integrates the dynamic conformational regulation of molecules with targeting functionality through synergistic effects. As shown in Scheme 1, environmental viscosity regulates the excited-state energy dissipation pathway by restricting the rotational freedom of TPA around the C–N single bond. Under low-viscosity conditions, free rotation promotes non-planar conformations in which excited-state energy dissipates *via* non-radiative transitions, resulting in weak fluorescence. In high-viscosity environments, restricted molecular motion drives D–A modules towards coplanar conformations, and increased molecular orbital overlap enhances radiative transitions in the near-infrared (NIR) region, achieving responsiveness to viscosity. Lysosomal targeting employs a hydrophobic-driven mechanism. Lysosomal membranes are predominantly composed of cholesterol and specific lipids, so their hydrophobic properties are highly matched to hydrophobic groups. Harnessing the marked hydrophobicity of TPA, this mechanism traverses the membrane architecture to anchor within the hydrophobic domain of the lipid bilayer, enabling surface enrichment. This strategy functions independently of pH parameters, avoiding the dependence of conventional probes on lysosomal acidity while precluding monitoring interference caused by alkalisation. Thus, the probe **LTP-H** serves as an effective tool for monitoring viscosity changes.

3.2 Mechanism for sensing viscosity by the probe TLP-H

To elucidate the response mechanism of the probe to viscosity, we conducted a series of quantum chemical calculations based
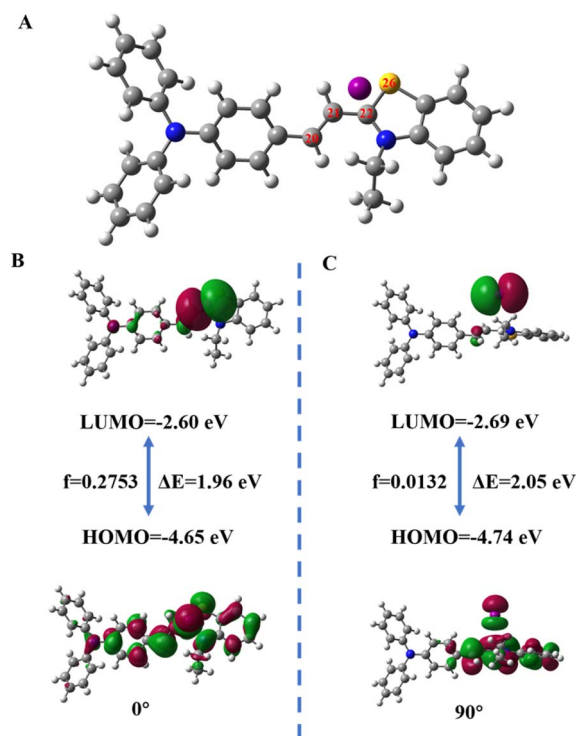

Fig. 1 (A) Optimised geometry of **LTP-H** in the excited state. (B) Frontier molecular orbitals of **LTP-H** in the excited state with a dihedral angle of 0° near C20−C21−C22−N26. (C) Frontier molecular orbitals of **LTP-H** in the excited state with a dihedral angle of 90° near C20−C21−C22−N26 with a 90° dihedral angle in the vicinity (f: oscillator strength).

on density functional theory (DFT) and time-dependent density functional theory (TD-DFT) using the software Gaussian09 and B3LYP/6-31G(d,p) basis set. The initial geometry of the probe **LTP-H** was generated using the software Gaussian View (Fig. 1A). Under high-viscosity conditions, the probe **LTP-H** adopted a planar conformation with a dihedral angle of 0°, where the HOMO orbital was highly localized in the π-conjugated system of the triphenylamine donor; whereas the LUMO orbital was concentrated in the electron-deficient heterocyclic ring of the benzothiazole acceptor. The significant spatial separation of the donor–acceptor orbital distribution formed an efficient charge transfer channel, resulting in a strong charge transfer transition (oscillator strength of 0.2753), which was manifested as high-intensity fluorescence emission (Fig. 1B). When the environmental viscosity decreased, the rotational freedom of the single bond within the molecule increased, and the dihedral angle of the probe **LTP-H** rotated to 90° to form an orthogonal conformation. This action led to the HOMO being localized in the isolated aromatic ring of triphenylamine and the LUMO being confined to the thiazole unit of the benzothiazole, blocking the conjugated channel. At this point, the oscillator strength dropped from 0.2753 at the 0° dihedral angle near C20−C21−C22−N26 to 0.0132 at the 90° dihedral angle (Fig. 1C). These results indicated that intramolecular rotation caused the probe to form a distorted excited state, resulting in

weak fluorescence emission, confirming the TICT mechanism of the probe.

3.3 Spectral characteristics of the probe LTP-H

To systematically explore the relationship between the photophysical properties of the probe **LTP-H** and the viscosity of the medium, glycerol and methanol were initially chosen as representative solvent systems for spectroscopic analysis. The probe indicated characteristic absorption peaks at 570 nm in both methanol and glycerol. When an excitation wavelength of 570 nm was used, only a faint fluorescence signal was observed in the methanol system, whereas the glycerol system showed a significantly enhanced emission peak at 650 nm with a Stokes shift of 83 nm and a 93-fold rise in the fluorescence signal (Fig. 2A and B). This change could be attributed to the viscosity-dependent molecular conformational regulation mechanism. That is, in low-viscosity media, the intramolecular rotational freedom of the probe was high, and the excited state energy was rapidly dissipated through non-crossing. In high-viscosity environments, the blockade of molecular torsional motion induced donor–acceptor modules to converge to co-planar arrangements, which effectively expanded the π-electronic conjugation system, thus increasing the probability of radiative transitions and significantly enhancing the fluorescence signal. To further assess the viscosity response and sensitivity of the probes, a glycerol–methanol binary solvent gradient system

(viscosity range of 1.30–938.0 cp) was further constructed. Fig. 2C shows that the fluorescence signal at 650 nm displayed an exponential growth trend as the glycerol volume fraction increased from 0% to 100%, indicating that the probe had an ultrasensitive response to the high-viscosity microenvironment. As shown in Fig. 2D, an excellent linear correlation ($R^2 = 0.995$) was presented by linearly fitting its probe emission intensity ($\log I_{650}$) to the medium viscosity ($\log \eta$), which suggested an excellent viscosity responsiveness of the probe **LTP-H** and that it had unique capability for detecting viscosity changes in an external environment.

In order to analyse the interference of polarity on the probe, the spectral response behaviour of the probe in different polar solvents was subsequently tested. In the UV spectra (Fig. 3A), we observed a slight bathochromic shift in the absorption wavelengths of the different solvents in the range of 560–575 nm, which was caused by changes in viscosity and molecular conformation. That is, the molecules were free to rotate at low viscosities triggering a conjugate shortening blue shift, whereas high viscosities restricted the rotation, leading to a conjugate planarisation bathochromic shift; polar solvents could also be red-shifted by stabilising the excited state charge separation (solvatochromic effect). In addition, the nature of the solvent and multiple interactions between the probe molecules and solvent also led to differences in absorbance in different solvents. That is, high polarity enhanced the absorbance through strong solvation by increasing the concentration of
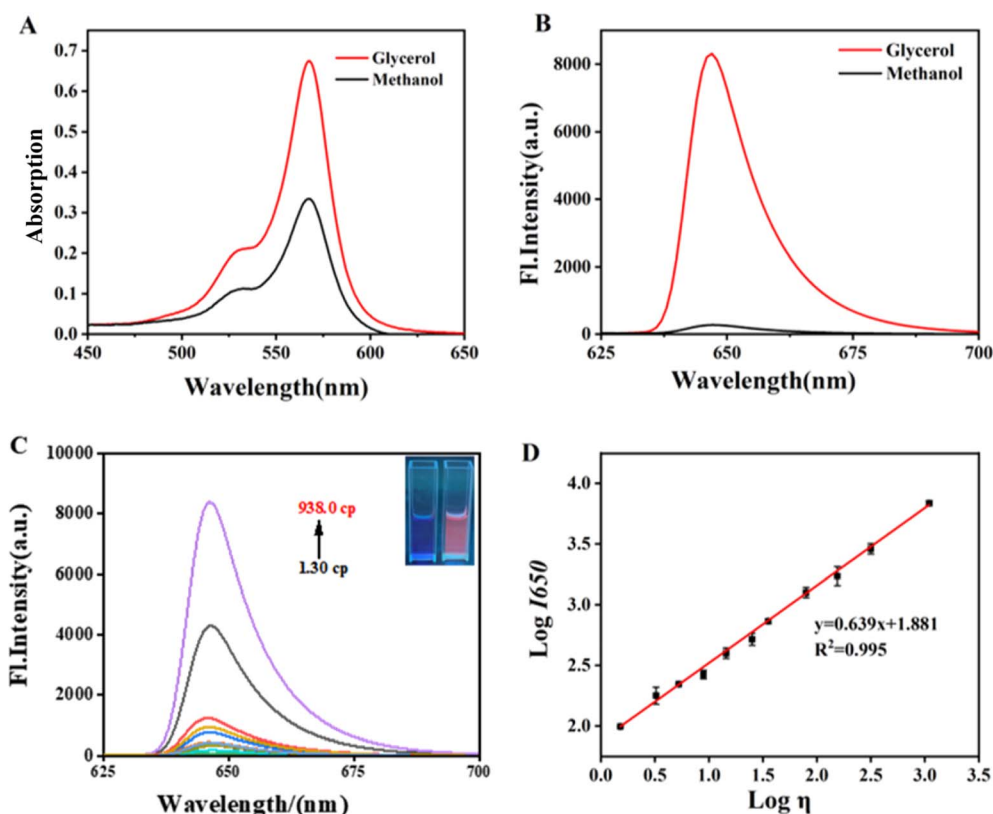

Fig. 2 (A) UV-vis spectrum of **LTP-H** (10 μM) in MeOH and Gly. (B) FL spectra of **LTP-H** (10 μM) in MeOH and Gly. (C) FL spectra of **LTP-H** (10 μM) with variation of the solution viscosity (1.30–938.0 cp). (D) Linear correlation between $\log I_{650}$ and $\log \eta$; λ_{ex} = 570 nm, λ_{em} = 650 nm.
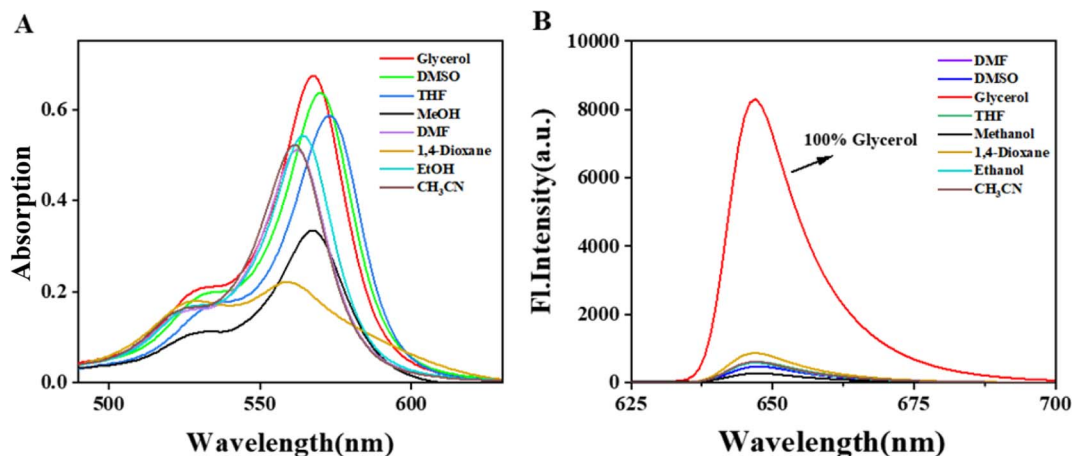
Fig. 3 (A) UV-vis spectrum of LTP-H (10 µM) in distinct polar solvents. (B) Fluorescence spectrum of LTP-H (10 µM) in distinct polar solvents. $\lambda_{ex} = 570$ nm, $\lambda_{em} = 650$ nm.

chromophores and the probability of electron transition. Low polarity induced molecular aggregation to weaken the absorption peaks, the dynamic effect of which was amplified by modulation of the molar absorption coefficients. In addition,

interactions between the probe molecules and solvent (*e.g.*, hydrogen bonding) could lead to a bathochromic shift by limiting conjugated electron delocalisation, which caused a variation in absorbance by limiting the conjugated electrons
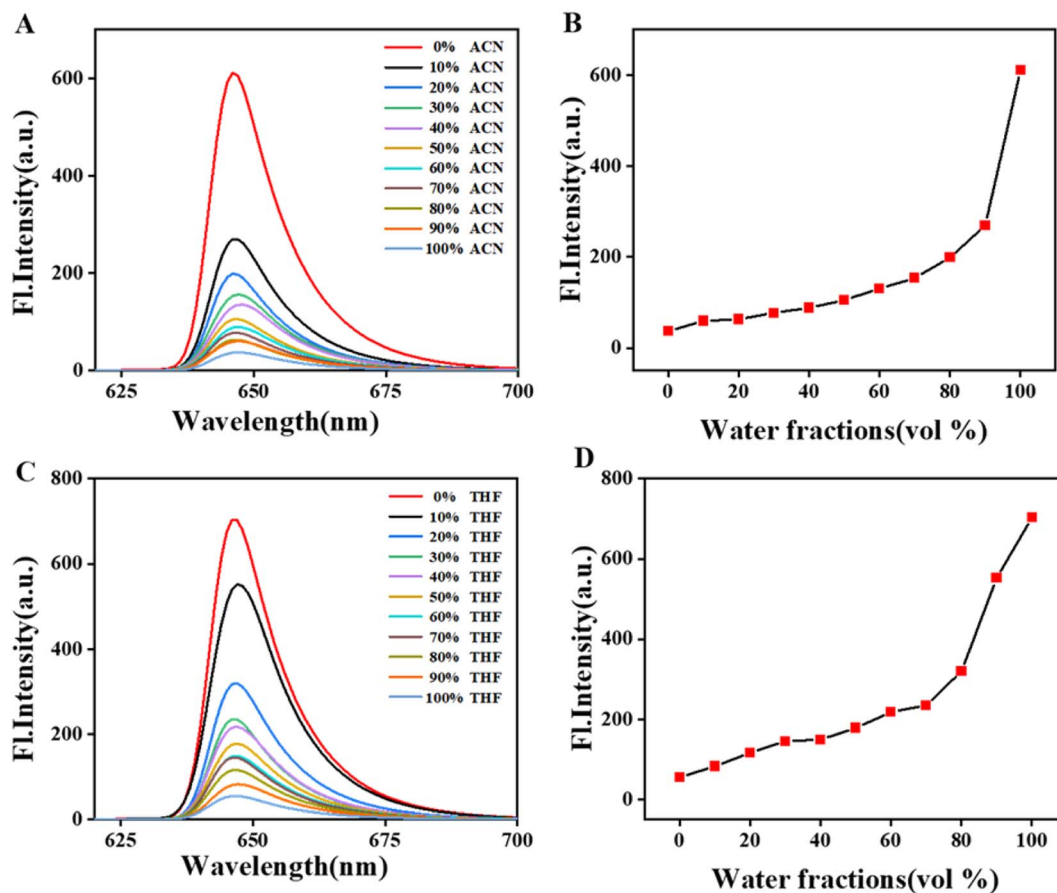

Fig. 4 (A) Fluorescence spectra of the probe LTP-H in a water−acetonitrile system; (B) plot of the maximum fluorescence intensity of the probe LTP-H in a water−acetonitrile system *versus* water volume fraction. (C) Fluorescence spectra of the probe LTP-H in a water−tetrahydrofuran system. (D) Plot of maximum fluorescence intensity of the probe LTP-H in a water−tetrahydrofuran system *versus* water volume fraction.
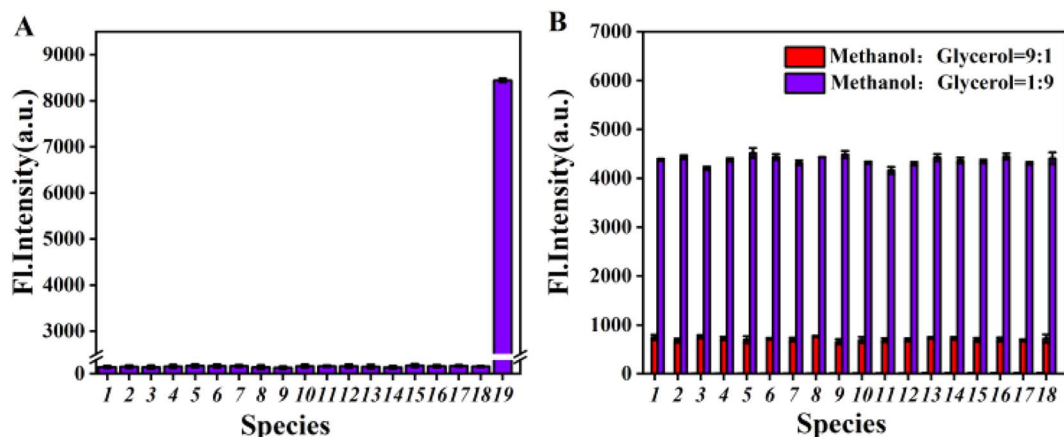
Fig. 5 (A) Selectivity experiments with the probe LTP-H (10 µM). (B) Fluorescence spectrum of LTP-H (10 µM) with the addition of analytes in two viscosity systems (fluorescence intensity at 650 nm). (1) Blank. (2) Fe^{2+}. (3) Fe^{3+}. (4) Co^{2+}. (5) Hg^+. (6) Ca^{2+}. (7) Mg^{2+}. (8) F^-. (9) SCN^-. (10) $H_2PO_4^-$. (11) SO_4^{2-}. (12) CO_3^{2-}. (13) $ONOO^-$. (14) HClO. (15) HSO_3^-. (16) $S_2O_3^{2-}$. (17) Hcy. (18) Ser. (19) Glycerol. $\lambda_{ex} = 570$ nm, $\lambda_{em} = 650$ nm.

from the domain. In the fluorescence spectra (Fig. 3B), minimal signal changes were observed for the probe LTP-H in different solvents, and its fluorescence emission intensity was weak and remained at a low level. However, after the introduction of glycerol, the fluorescence signal intensity at 650 nm increased

93-fold with a quantum yield of 61.50% (2.01% for methanol). Comparison of the UV absorption spectral parameters of the probe LTP-H in different solvents with the change in fluorescence intensity (ESI Table 1†) revealed the magnitude of the former change to be almost negligible. This phenomenon
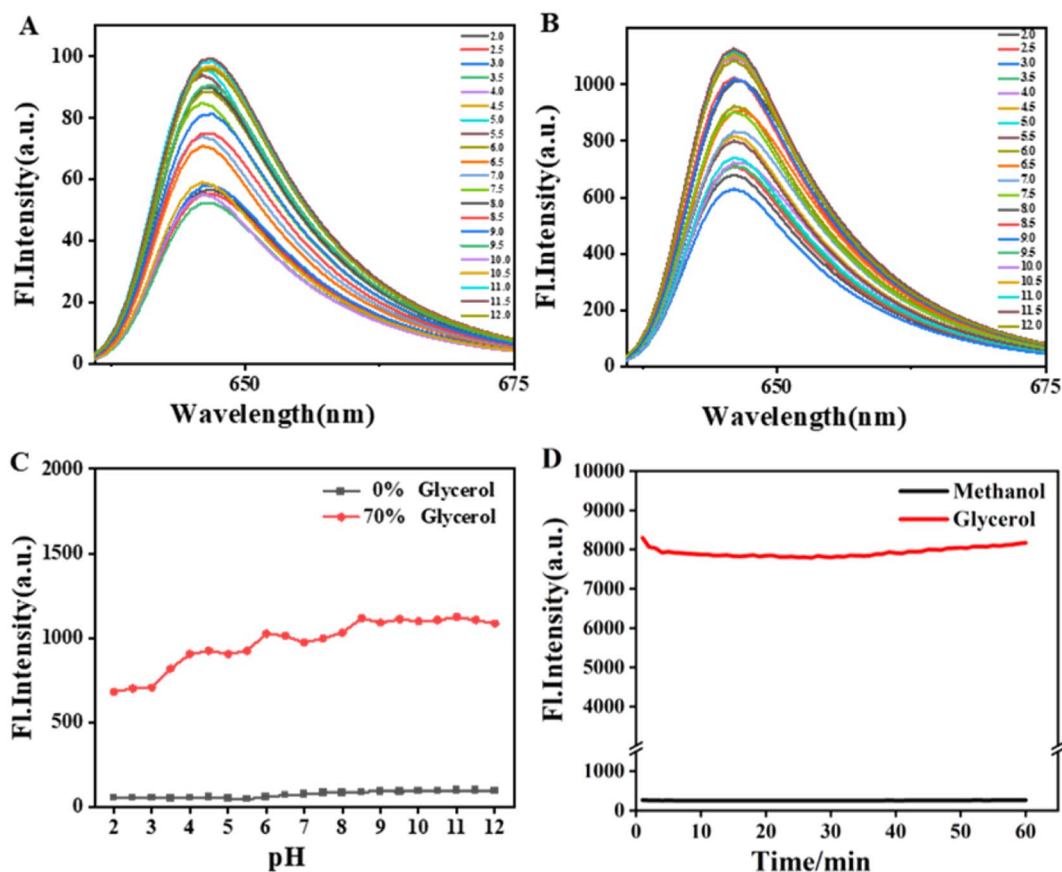

Fig. 6 (A) Fluorescence signal of LTP-H (10 µM) in a pH-buffer liquid system of pure methanol. (B) Fluorescence signal of LTP-H (10 µM) in a pH-buffer liquid system with 70% glycerol. (C) Fluorescence signal of LTP-H (10 µM) in pH systems with different viscosities. (D) Photostability of LTP-H (10 µM) under constant laser exposure in glycerol and methanol (60 min). $\lambda_{ex} = 570$ nm, $\lambda_{em} = 650$ nm.
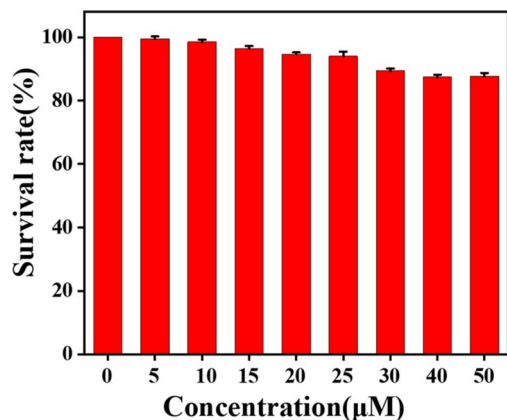
Fig. 7 Toxic responses of HepG2 cells to graded concentrations of the probe LTP-H.

clearly revealed that the luminescence mechanism of the probe LTP-H was typically viscosity-dependent, and that the solvent polarity parameter had a negligible effect on its fluorescence behaviour. These features make it effective for the detection of complex biological microenvironments to avoid the interference of a polar background.

Based on the triphenylamine (TPA) moiety, a classical AIE active unit which is present in the LTP-H probe, we sought to systematically ascertain if it aggregates to induce luminescence properties. We chose different ratios of the mixed systems of water–acetonitrile (polar system) and water–tetrahydrofuran (non-polar system) as the test media, and systematically observed the effect of water content (0–100%, v/v) on the fluorescence behaviour of the probes. The fluorescence intensity did not change significantly if the water content was low. However, if the water content was increased to 90% (water–acetonitrile system) and 80% (water–tetrahydrofuran system), the fluorescence intensity of the two systems increased significantly (16.5-fold and 13.4-fold, respectively). These data indicated that the probe molecules gradually showed aggregation in the system, triggering fluorescence activation in aggregated states, resulting in fluorescence activation of the probes (Fig. 4A and C) and in a change of fluorescence intensity (Fig. 4B and D). This phenomenon was attributed to the synergistic effect of restricted intramolecular motion and donor–acceptor synergistic charge transfer. In the dispersed state, the benzene ring of triphenylamine consumed the excited state energy due to free rotation, resulting in weak fluorescence. In the aggregated state, the spatial resistance formed by intermolecular π–π stacking and van der Waals forces "froze" the rotation of the benzene ring, forcing energy release by radiative transfer. At the same time, the rigid planar structure of benzothiazole effectively reduced excessive π–π stacking to prevent aggregation-caused quenching (ACQ), while simultaneously forming an ordered donor–acceptor (D–A) configuration. This optimized structure enabled efficient charge transfer between triphenylamine and benzothiazole, with significantly enhanced radiative emission
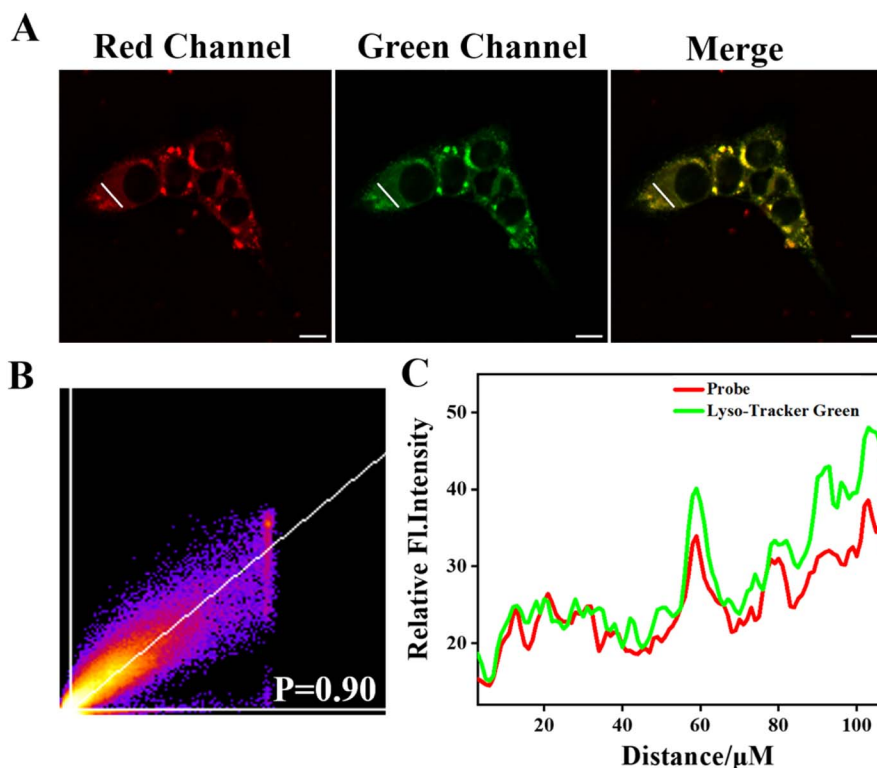

Fig. 8 (A) Co-localisation imaging of the probe LTP-H (10 μM) with LysoTracker™ Green (10 μM) in HepG-2 cells; red channel (λ_{ex} = 590 nm, λ_{em} = 560–700 nm); green channel (λ_{ex} = 488 nm, λ_{em} = 500–550 nm). (B) Correlation of the distribution of red-channel and green-channel fluorescence intensity. (C) Map showing the cellular ROI fluorescence intensity distribution. Scale bar: 10 μm.

in the aggregated state. Thus, the probe **LTP-H** had the characteristics of AIE, which is beneficial for subsequent bioimaging to maintain a stable effect.

To systematically evaluate the specific responsiveness of the probe **LTP-H** in complex biological systems, a test system was constructed to cover five typical types of interferers. The latter included common metal ions (Fe^{2+}, Fe^{3+}, Co^{2+}, Hg^+, Ca^{2+}, Mg^{2+}), inorganic anions (F^-, SCN^-, $H_2PO_4^-$, SO_4^{2-}, CO_3^{2-}), reactive oxygen/nitrogen species (ONOO–, HClO), sulfur-containing reactive species (HSO_3^-, $S_2O_3^{2-}$), and amino acids (Hcy, Ser, Leu). The introduction of the above interferences into the methanol masterbatch of the probe resulted in almost unchanged fluorescence intensity fluctuations at 650 nm and remained at a low fluorescence intensity level, suggesting that the probe exhibited exceptional performance against common interferences. The fluorescence intensity of the probe in glycerol was increased 83-fold compared with that of the interfering system, showing a remarkable viscosity-specific response (Fig. 5A). This selective mechanism was further validated through a binary solvent gradient experiment (methanol : glycerol = 9 : 1 to 1 : 9). The fluorescence intensity was marginally changed by the addition of selective ions to the same system; with an increase in the proportion of glycerol in the system and increase of viscosity, the contrast in fluorescence signal of the probe exhibited an enhancement (Fig. 5B). Collectively, these data suggested that the probe **LTP-H** was not affected by the interfering substances and displayed a significant viscosity-specific response, so it could be utilised as a sensitive viscosity detection probe.

The experimental evidence established **LTP-H** as a reliable *in vitro* viscosity probe. Given the physiological pH heterogeneity, we systematically evaluated the pH susceptibility of **LTP-H** by setting up phosphate-buffer systems (pH = 2.0–12.0) with different pH ranges and glycerol-buffer systems (0% and 70%) with controlled viscosities. As presented in Fig. 6A and B, fluctuation of the fluorescence intensity at 650 nm of the probe with pH change did not change significantly under the condition of constant viscosity. When the viscosity of the system was elevated, the pH insensitivity was maintained and the fluorescence intensity was enhanced. These phenomena were related to the chemical stability and charge distribution of the **LTP-H** molecular structure. Protonation or deprotonation at the tertiary amine structure at the triphenylamine donor end of the probe was difficult due to spatial resistance and electron cloud characteristics, and the acceptor end of the benzothiazole was quaternised to form a steady-state positive charge centre whose charge characteristics were completely independent of the changes in the acid–base environment. The chemical inertness of iodide ions makes them resistant to hydrolysis/coordination over a wide pH range. Together, the above factors strengthened the pH stability of the system and confirmed that the probe luminescence mechanism was independent of the protonation state, and demonstrated strong tolerance to changes in the ambient pH environment (Fig. 6C). Finally, an accelerated light ageing experiment by continuous xenon lamp irradiation simulated the detection conditions of the pure methanol/ glycerol system demonstrated that the fluorescence spectral
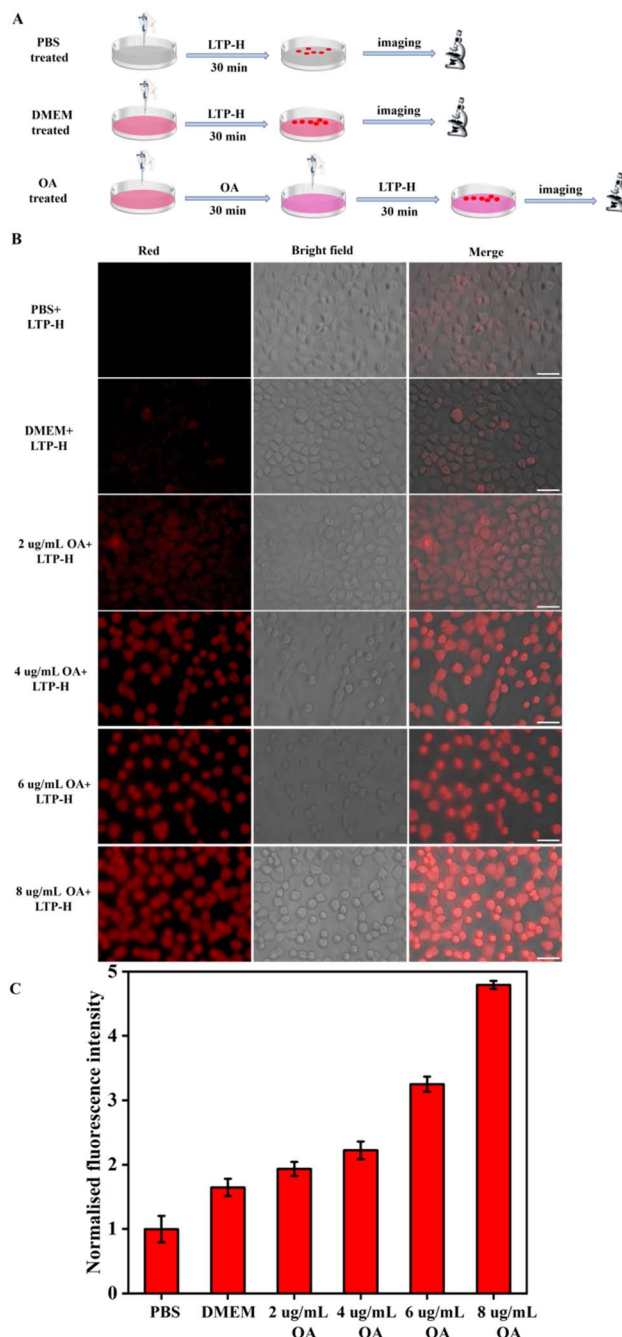

Fig. 9 (A) OA-induced inflammatory HepG-2 cells detected by the probe **LTP-H** (schematic). (B) Viscosity test for HepG2 cells. From top to bottom: incubation with PBS and **LTP-H** (10 μM) for 30 min only; incubation with DMEM and **LTP-H** (10 μM) for 30 min only; incubation with OA (2, 4, 6 and 8 μg mL^{-1}) for 1 h treated with **LTP-H** (10 μM) for 30 min. From left to right: red fluorescence channel field; bright field; superimposed field. (C) Normalised quantitative fluorescence intensity of HepG2 cells in confocal microscopic imaging. Normalised baseline values are fluorescence intensities for the PBS group. λ_{ex} = 570 nm, λ_{em} = 590–700 nm. Scale bar: 20 μm.

signals remained constant during 60 min of dynamic monitoring, confirming that the probe possessed excellent photostability characteristics (Fig. 6D). Comprehensive spectroscopic
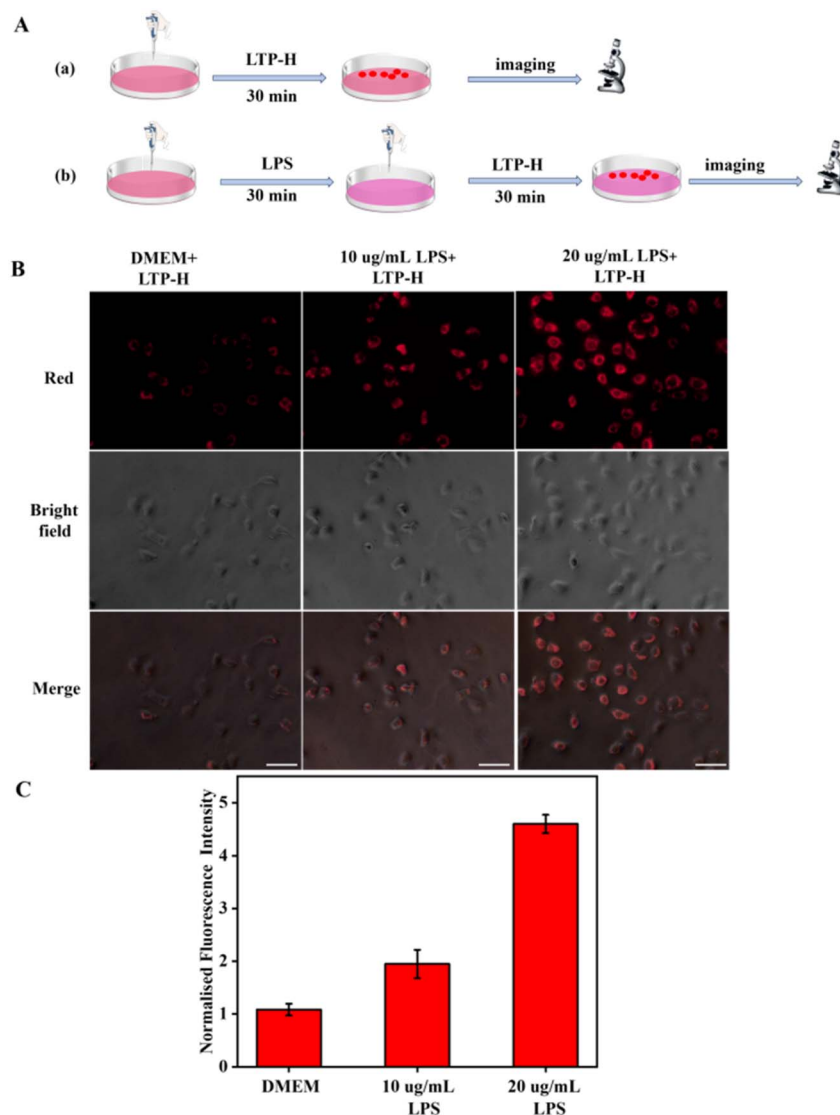
Fig. 10   (A) Use of the probe **LTP-H** for detecting LPS-induced HepG2 cells (schematic). (B) Viscosity test for HepG2 cells. From left to right: incubation with DMEM and **LTP-H** (10 μM) for 30 min only; incubation with LPS (10 and 20 μg mL^{-1}) for 1 h treated with **LTP-H** (10 μM) for 30 min. From top to bottom: red fluorescence channel field; bright field; superimposed field. (C) Normalized quantitative fluorescence intensity of HepG2 cells in confocal microscopic imaging; normalised baseline values are fluorescence intensities for the DMEM group. λ_{ex} = 570 nm, λ_{em} = 590–700 nm. Scale bar: 20 μm.

test results showed that the probe **LTP-H** had the advantages of viscosity-specific response, anti-interference, pH stability and optical stability. These features make it suitable for long-term tracking of intracellular viscosity changes for monitoring and research.

3.4   Fluorescence imaging of LTP-H in HepG2 cells

After the above spectroscopic study, we learnt that the probe **LTP-H** had excellent fluorescence properties in viscosity response and could be used in biological environments. Consequently, the probe was applied to detect viscosity in cells. To verify the biosafety of the **LTP-H** probe in cellular imaging, the toxic effect on HepG2 cells (Jiangsu Kaige Biotechnology Co., Ltd, China) was systematically evaluated using the MTT

assay. Concentration gradients of the probe (0, 5, 10, 15, 20, 25, 30, 40, and 50 μM) and cells were incubated together for 24 h. The results demonstrated (Fig. 7) that even in the group exhibiting the highest concentration (50 μM), the percentage of cells that survived was 87% (substantially exceeding the working concentration of 5–10 μM required for conventional imaging). Hence, the probe **LTP-H** had low toxicity and was applicable to prolonged live-cell monitoring and imaging applications.

Lysosomal membranes are predominantly composed of cholesterol and specific lipids, forming a dense, low-mobility hydrophobic core through close packing.[43] Hydrophobic groups (*e.g.*, aromatic rings, alkyl chains), which exhibit high compatibility with the hydrophobicity of lysosomal membrane lipids, can be incorporated into the membrane lipid layer *via*

intermolecular forces,[44] significantly reducing permeation resistance and facilitating entry into lysosomes by passive diffusion.[45] Based on the strong hydrophobic effect of the TPA moiety in probe **LTP-H** it was inferred to have lysosomal targeting potential. To verify its feasibility, lysosomal co-targeting experiments were performed. HepG-2 cells were pretreated with the probe **LTP-H** for 30 min, then incubated with lysosomal co-localisation dye LysoTracker™ Green for 30 min, and imaging was performed. The spatial distribution of the red fluorescence of probe **LTP-H** and the green fluorescence of the lysosomal co-localisation dye LysoTracker Green were highly consistent with each other (Fig. 8A), with a Pearson co-localisation coefficient as high as 0.90 (Fig. 8B). In addition, the intensity trends of **LTP-H** and LysoTracker Green in the cellular ROI region were closely related (Fig. 8C). These experimental results demonstrated that the probe **LTP-H** could selectively target lysosomes and was utilised to monitor viscosity variations in lysosomes. Notably, due to the absence of basic (*e.g.*, amino) groups in the probe and the proton inertness of the benzothiazole salts, its enrichment in the lysosomal lumen (pH = 4.5–5.5) is difficult to achieve by protonation. Instead, the hydrophobic dominance of the TPA group directed the probe into the hydrophobic region of the lysosomal membrane and enriched it at the membrane surface. Compared with traditional acidic environment-dependent probes, the localisation mechanism of the probe **LTP-H** was completely independent of lysosomal pH fluctuations, which could effectively circumvent the failure in lysosomal localisation caused by the alkalinisation effect.

Oleic acid can interact with cellular receptors, activate inflammatory pathways, produce reactive oxygen species, and disturb lipid metabolism.[46] If triggered by inflammation, oleic acid can alter cell membrane fluidity, induce cytoskeletal remodelling, and cause intracellular aggregation, which have been reported to collectively lead to the rise in cellular viscosity.[47] We wished to investigate whether the probe **LTP-H** could effectively distinguish normal cells from inflammatory cells. We induced inflammation in HepG2 cells using different concentrations of oleic acid to observe the response of the probe to viscosity changes. The cells were divided into three groups. The first group was treated with PBS for 3 h followed by a 30 min incubation with the probe **LTP-H**. The second group was first incubated with DMEM for 12 h and then treated with the probe for 30 min. The third group was exposed to increasing concentrations of oleic acid (2, 4, 6, and 8 μg mL^{-1}) for 1 h to induce inflammation, followed by a 30 min incubation with the probe for imaging. The PBS-treated group exhibited reduced metabolic activity and biomolecule synthesis, leading to decreased cellular viscosity and consequently displaying minimal red-channel fluorescence. In contrast, the DMEM-treated group (serving as a medium control), exhibited normal biosynthetic activity, resulting in moderately stronger fluorescence intensity in the red channel compared with that of the PBS group (Fig. 9A). Finally, the oleic acid-induced group had the strongest fluorescence signal, and its maximum fluorescence intensity was up to 4.8-fold and 3.6-fold of that of the PBS and DMEM-treated groups, respectively. This enhancement correlated with the gradual increase in oleic acid concentration, which amplified inflammatory responses and elevated cellular viscosity, thereby intensifying the red-channel fluorescence signal (Fig. 9B). These findings confirmed that the probe **LTP-H**
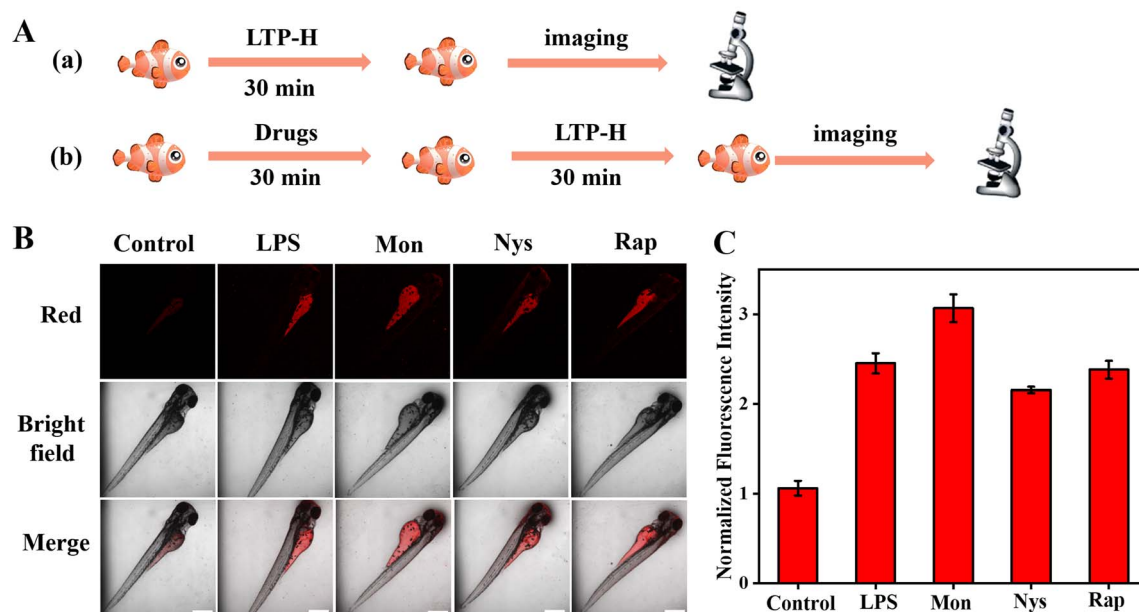
Fig. 11   (A) Imaging from the zebrafish viscosity experiment. (B) Confocal fluorescence images of the probe **LTP-H** (10 μM) in zebrafish. From left to right: zebrafish co-incubated with probe **LTP-H** for 30 min only; treated with lipopolysaccharide (10 μM), monensin (10 μM), nystatin (10 μM), and rapamycin (10 μM) for 30 min, respectively, followed by incubation with **LTP-H** for 30 min (10 μM). From top to bottom: red fluorescence channel view; bright field; superimposed view. (C) Normalised quantitative fluorescence intensity of zebrafish under the above conditions. Normalised baseline values are fluorescence intensities for the control group; λ_{ex} = 570 nm, λ_{em} = 590–700 nm. Scale bar: 20 μm.

could monitor intracellular viscosity changes while differentiating between normal cells and inflammatory cells.

Lipopolysaccharide (LPS), as a typical pathogen-associated molecule, triggers inflammation and oxidative stress through activation of cellular receptors, disrupting mitochondrial and lysosomal structures.[48] This leads to metabolite stasis, enzyme leakage, and localised viscosity elevation. Its induced abnormal lipid accumulation and oxidation products lead to the formation of a high-viscosity pathological zone, hindering material transport and energy metabolism.[49–51] This forces continuous activation of inflammatory signals, establishing a viscosity abnormality–inflammation vicious cycle. Based on these mechanisms, we employed an LPS-induced HepG2 cell inflammation model and monitored viscosity using the **LTP-H** probe. The red-channel fluorescence signal of the control (DMEM) group treated with only the **LTP-H** probe (10 μM) for 30 min was extremely weak (Fig. 10B), whereas the fluorescence intensity of HepG2 cells pre-treated with LPS for 30 min to induce inflammation increased significantly with the LPS concentration gradient (Fig. 10C), reaching 4.6-fold higher than the control group. These data confirmed that the probe **LTP-H** effectively detected a viscosity imbalance in LPS-stimulated cellular inflammation.

Zebrafish are highly genetically homologous to humans and are commonly used to model and study human diseases.[52–54] On this basis, we designed probe assay experiments for different drug-induced viscosity changes in zebrafish *in vivo* to validate the feasibility of the probe **LTP-H** for detecting viscosity changes in live animals. Zebrafish were incubated with different drugs (lipopolysaccharide, monensin, nystatin and rapamycin) to induce viscosity changes. Only weak red fluorescence was observed when zebrafish were treated with only **LTP-H** (10 μM). However, when zebrafish were treated with 10 μM lipopolysaccharide, monensin, mycoplasma, and rapamycin for 30 min, and then incubated with the probe (10 μM) for 30 min, fluorescence intensity was enhanced (Fig. 11B). We documented a 2.1-fold increase in the maximum normalised fluorescence intensity in the drug-treated group compared with that in the control group. These results showed that the **LTP-H** probe could effectively monitor viscosity changes in living animals. Hence, the probe could be a reliable molecular imaging tool for visualising and diagnosing inflammation-related diseases.

4. Conclusions

We rationally designed a lysosomal viscosity-targeting fluorescent probe (**LTP-H**) based on the TICT mechanism for detecting inflammation in organisms. The probe was readily synthesised and exhibited excellent photophysical properties at 650 nm, including a good linear relationship ($R^2 = 0.995$), high resistance to interference (non-responsive to pH variations, small biomolecules, or ions), and high photostability, with a 93-fold viscosity response enhancement compared with methanol. Diverging from conventional probes, **LTP-H** accomplished pH-independent precision targeting of lysosomes ($P = 0.90$) through the pronounced hydrophobicity of the TPA backbone and employed a hydrophobicity-driven penetration localisation

strategy, circumventing the reliance of traditional probes on acidic microenvironments while preventing interference from alkalisation. Bioimaging experiments further demonstrated its capability to differentiate normal cells from inflammatory cells and monitor drug-induced viscosity changes in zebrafish, establishing a cross-scale viscosity monitoring system spanning *in vitro* to *in vivo* models. Therefore, the probe **LTP-H** provides a novel strategy for developing non-pH-dependent organelle probes, but also demonstrates good application prospects in diagnosing inflammatory states and investigating their underlying mechanisms.

Data availability

Data will be made available upon reasonable request.

Author contributions

Song Han: writing (original draft), methodology, investigation, and visualization. Xinying Jing: writing (original draft, review and editing), methodology, and investigation. Hui Peng: investigation. Weiying Lin: supervision, writing (review and editing), resources, and funding acquisition.

Conflicts of interest

There are no conflicts of interest to declare.

Acknowledgements

References

1 L. Zhang, M. Yi, S. Zhong, J. Liu, X. Liu, T. Bing, N. Zhang, Y. Wei and D. Shangguan, *Spectrochim. Acta, Part A*, 2022, **265**, 120394.

2 Y. Gao, J. Qiu, M. Liu, X. Xiong and H. Zhu, *Chem. Eng. J.*, 2023, **466**, 143100.

3 R. Kotani, H. Sotome, H. Okajima, S. Yokoyama, Y. Nakaike, A. Kashiwagi, C. Mori, Y. Nakada, S. Yamaguchi, A. Osuka, A. Sakamoto, H. Miyasaka and S. Saito, *J. Mater. Chem. C*, 2017, **5**, 5248–5256.

4 D. Martinez-Bourget, E. Rocha, P. Labra-Vazquez, R. Santillan, B. Ortiz-Lopez, V. Ortiz-Navarrete, V. Maraval, R. Chauvin and N. Farfan, *Spectrochim. Acta, Part A*, 2022, **283**, 121704.

5 M. Ren, B. Deng, X. Kong, K. Zhou, K. Liu, G. Xu and W. Lin, *Chem. Commun.*, 2016, **52**, 6415–6418.

6 C. Peng, X. Ma, D. Lin, X. Feng, H. Yu and Y. Li, *Anal. Chim. Acta*, 2021, **1187**, 339146.

7 Z. Yang, Y. Huo, Y. Liu, G. Du, W. Zhang, L. Zhou, L. Zhan, X. Ren, W. Duan and S. Gong, *RSC Adv.*, 2019, **9**, 32219–32225.

8 S. Ishii, A. Matsuura and E. Itakura, *Sci. Rep.*, 2019, **9**, 11635.

9 M. Li, J. Fan, H. Li, J. Du, S. Long and X. Peng, *Biomaterials*, 2018, **164**, 98–105.

10 D. Cao, L. Zhu, Z. Liu and W. Lin, *J. Photochem. Photobiol., C*, 2020, **44**, 100371.

11 Y. Zhang, Q. Liu, T. Tian, C. Xu, P. Yang, L. Ma, Y. Hou, H. Zhou and Y. Gan, *Sens. Actuators, B*, 2024, **399**, 134809.

12 G. Feng, Z. Li, P. Zhai, M. Ying, Z. Xu, C. Yang, X. Wang, B. Dong, K.-T. Yong and G. Xu, *Sens. Actuators, B*, 2022, **371**, 132577.

13 W. Ge, H. Wang, X. Wu, B. Dong, R. Zhang and M. Tian, *Anal. Chem.*, 2023, **95**, 14787–14796.

14 V. N. Nguyen and H. Li, *Molecules*, 2023, **28**, 6650.

15 L. Xu, F. Xiong, M. Kang, Y. Huang and K. Wu, *Analyst*, 2022, **147**, 4132–4140.

16 J. Lv, Q. Wei, X. Gong, E. Du and S. Zhang, *Sens. Actuators, B*, 2025, **422**, 136676.

17 L. Yuan, W. Lin, Z. Cao, J. Wang and B. Chen, *Chemistry*, 2012, **18**, 1247–1255.

18 H. J. Liu, M. S. Zhu, G. Zhang, R. Sun, Y. J. Xu and J. F. Ge, *Analyst*, 2023, **148**, 4463–4469.

19 L. Yuan, W. Lin, Y. Xie, B. Chen and J. Song, *Chem. Commun.*, 2011, **47**, 9372–9374.

20 Y. Xing, M. M. Wang, F. Zhang, T. Xin, X. Wang, R. Chen, Z. Sui, Y. Dong, D. Xu, X. Qian, Q. Lu, Q. Li, W. Cai, M. Hu, Y. Wang, J. L. Cao, D. Cui, J. Qi and W. Wang, *Nat. Commun.*, 2025, **16**, 985.

21 W. Lin, L. Yuan, J. Feng and X. Cao, *Eur. J. Org Chem.*, 2008, **2008**, 2689–2692.

22 L. Su, P. Hu, X. Luo, H. Ding, R. Zhang, Y. Qian, S. Qi, X. Tian and W. Ling, *ACS Appl. Mater. Interfaces*, 2025, **17**, 607–616.

23 S. Su, L. Chai, Q. An, W. Hu, L. Wang, X. Li, H. Zhang and C. Li, *Anal. Chem.*, 2022, **94**, 15146–15154.

24 Y. Li, Z. Wu, Z. Huang, C. Yin, H. Tian and X. Ma, *Natl. Sci. Rev.*, 2025, **12**, nwae383.

25 L. Fan, Y. Pan, W. Li, Y. Xu, Y. Duan, R. Li, Y. Lv, H. Chen and Z. Yuan, *Anal. Chim. Acta*, 2021, **1149**, 338203.

26 S. A. Sankaranarayanan, D. N. Yadav, S. Yadav, A. Srivastava, S. R. Pramatha, V. R. Kotagiri, H. Joshi and A. K. Rengan, *Langmuir*, 2024, **40**, 16743–16756.

27 T. Jin, C. Huang, M. Cui, Y. Yang, Z. Wang, W. Zhu and X. Qian, *J. Mater. Chem. B*, 2020, **8**, 10686–10699.

28 A. Bonardi, F. Bonardi, G. Noirbent, F. Dumur, C. Dietlin, D. Gigmes, J.-P. Fouassier and J. Lalevée, *Polym. Chem.*, 2019, **10**, 6505–6514.

29 M.-J. Hou, J.-T. Chen, W.-L. Jiang, G.-F. Zeng, J. Zhan, G.-J. Mao and C.-Y. Li, *Sens. Actuators, B*, 2022, **369**, 133286.

30 X. Wang, X. Wang, Q. Lu, X. Sun and Q. Han, *Spectrochim. Acta, Part A*, 2023, **296**, 122661.

31 Z. Peng, D. Zhang, H. Yang, Z. Zhou, F. Wang, Z. Wang, J. Ren and E. Wang, *Analyst*, 2024, **149**, 3356–3362.

32 H. Ma, Z. Luo, J. Ding, D. Zhang, F. Wang, H. Yu, W. Chen, J. Ren and E. Wang, *Sens. Actuators, B*, 2025, **424**, 136926.

33 Z. Wang, Z. Gao, Y. Gao, X. Pang and X. Xia, *Tetrahedron*, 2025, **179**, 134615.

34 Z. Wu, T. Zhao, X. Jiang, D. Zhang, F. Wang, X. Ren, Z. Wang, E. Wang and J. Ren, *Anal. Bioanal. Chem.*, 2024, **416**, 6485–6495.

35 A. Ren, L. Qiao, K. Li, D. Zhu and Y. Zhang, *Anal. Bioanal. Chem.*, 2024, **416**, 6223–6235.

36 P. Zhang, W. Meng, L. Wei, Y. Li, H. Xiao, Y. He, F. Yang, X. Han and W. Shu, *Food Chem.*, 2024, **460**, 140527.

37 Q. Wang, Y.-X. He, Y.-X. Wu, X.-F. Wang, D.-Q. Zhang and J.-J. Li, *Dyes Pigm.*, 2024, **231**, 112416.

38 L. Chao, G. Aodeng, L. Ga and J. Ai, *Microchem. J.*, 2025, **208**, 112535.

39 J. Hao, X. Li, S. Shi, H. Zhang, H. Zhu, J. Wu, M. Gao and B. Zhang, *Bioorg. Chem.*, 2025, **155**, 108162.

40 H. Ke, J. Yang, W. Zhang, P. Yang, Y. Wang, N. Wang, J. Bai, H. Yin, Y. Chen, X. Chen, P. Fu, Y. Gan, G. Zang and Q. Liu, *Biosens. Bioelectron.*, 2025, **277**, 117285.

41 D. Paderni, D. Lopez, A. Ciavarella, M. Montanari, G. Panza, M. Voccia, M. Formica, B. Canonico, E. Macedi, S. Papa and V. Fusi, *Inorg. Chim. Acta*, 2025, **581**, 122620.

42 Y. J. Kim, M. Jang, J. Roh, Y. J. Lee, H. J. Moon, J. Byun, J. Wi, S. K. Ko and J. Tae, *Int. J. Mol. Sci.*, 2023, **24**, 15073.

43 M. Stark, T. F. D. Silva, G. Levin, M. Machuqueiro and Y. G. Assaraf, *Cells*, 2020, **9**, 1082.

44 C. S. Abeywickrama, K. J. Wijesinghe, R. V. Stahelin and Y. Pang, *Chem. Commun.*, 2019, **55**, 3469–3472.

45 B. Zhitomirsky, A. Yunaev, R. Kreiserman, A. Kaplan, M. Stark and Y. G. Assaraf, *Cell Death Dis.*, 2018, **9**, 1191.

46 J. Li, H. Rao, Q. Bin, Y. W. Fan, H. Y. Li and Z. Y. Deng, *Eur. J. Lipid Sci. Technol.*, 2016, **119**, 1600374.

47 D. H. Lee, J. Ahn, Y. J. Jang, T. Y. Ha and C. H. Jung, *Biochem. Biophys. Res. Commun.*, 2019, **513**, 553–559.

48 C. de la Haba, A. Morros, P. Martinez and J. R. Palacio, *J. Membr. Biol.*, 2016, **249**, 789–800.

49 R. Guo, J. Yin, Y. Ma, Q. Wang and W. Lin, *J. Mater. Chem. B*, 2018, **6**, 2894–2900.

50 Y. Zhou, T. Jin, M. Gao, Z. Luo, S. Mutahir, C. Shi, T. Xie, L. Lin, J. Xu, Y. Liao, M. Chen, H. Deng, M. Zheng and J. Shan, *Chin. Med.*, 2023, **18**, 36.

51 R. Wen, T. N. Zhang, T. Zhang, Y. J. Tong, W. L. Song, Y. P. Liu, N. Yang and C. F. Liu, *FASEB J.*, 2023, **37**, e23063.

52 H. Zheng, G. Li, L. Zhang, M. Fan and W. Lin, *New J. Chem.*, 2024, **48**, 16710–16717.

53 T. O. C. Moll and S. A. Farber, *Arterioscler., Thromb., Vasc. Biol.*, 2024, **44**, 1053–1064.

54 Y. Liu, J. Nie, J. Niu, W. Wang and W. Lin, *J. Mater. Chem. B*, 2018, **6**, 1973–1983.